NANO LETTERS

pubs.acs.org/NanoLett

Letter

Substrate Curvature Enhances Molecular Electrocatalysts for the Efficient Production of Hydrogen Peroxide

Chunxiao Liu, Qiuxu Chen, Zhaoyang Chen, Jinge Wang, Haoyuan Wang, Laihao Luo, Xu Li, Qiu Jiang, Tingting Zheng,* and Chuan Xia*

Cite This: *Nano Lett.* 2025, 25, 16013−16019

Read Online

ACCESS | Metrics & More | Article Recommendations | Supporting Information

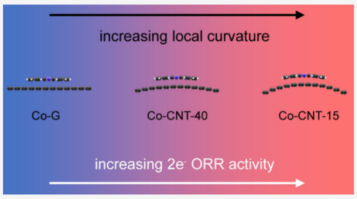

ABSTRACT: The two-electron oxygen reduction reaction ($2e^-$ ORR) offers a green alternative to the anthraquinone process but demands efficient catalysts. Here, we demonstrate substrate curvature as an independent design lever for $2e^-$ ORR catalysis. Cobalt phthalocyanine (CoPc) was immobilized on carbon supports of distinct geometries, i.e., planar graphene and carbon nanotubes with different diameters, to isolate the curvature effects. In alkaline flow cells, CoPc on 15 nm CNTs delivers a >15-fold higher turnover frequency than CoPc on graphene does and a maximum productivity of 73.9 mol g_{cat}^{-1} h^{-1}. *In situ* spectroscopy and density functional theory revealed curvature-induced strengthening of *OOH adsorption, lowering the barriers for H_2O_2 formation. When integrated into a 10 cm × 10 cm porous solid-electrolyte reactor, the optimal catalyst achieves >70% selectivity at 10 A and stable operation for more than 10 h. This validation positions curvature engineering as a predictable, tunable strategy for designing high-performance electrocatalysts.

KEYWORDS: *$2e^-$ O_2 electroreduction, H_2O_2 electrosynthesis, Co single atom, substrate curvature, porous solid-electrolyte reactor*

Hydrogen peroxide (H_2O_2), a versatile and environmentally benign oxidant, is indispensable across diverse sectors, including chemical synthesis, water treatment, and energy storage, with a global market projected to exceed $4 billion by 2027.[1] However, over 95% of H_2O_2 is produced *via* the anthraquinone process, which generates significant waste and requires high energy inputs due to multistep hydrogenation/oxidation cycles.[2−4] This method also necessitates centralized production facilities, incurring logistical costs and safety risks from H_2O_2 transport.[5] The electrocatalytic 2-electron oxygen reduction reaction ($2e^-$ ORR) offers a sustainable alternative by enabling decentralized, on-demand H_2O_2 synthesis using renewable electricity.[6−12] However, its viability hinges on the development of catalysts that simultaneously achieve high activity (>100 mA cm^{-2}), selectivity (>90%), and durability (>100 h) under industrial current densities.[13]

Transition metal-based molecular catalysts, particularly macrocyclic complexes, are attractive $2e^-$ ORR catalysts, as they provide atomically defined active sites and rich handles for tuning the *OOH binding that underpins $2e^-$ ORR selectivity.[14−19] Their primary coordination environments govern the ORR pathway: cobalt centers in *pyrrolic* Co−N_4 environments favor $2e^-$ reduction to H_2O_2, whereas *pyridinic* Co−N_4 sites tend to cleave the O−O bond and yield water *via* the $4e^-$ pathway.[19] Recent advances in substrate engineering have further highlighted the critical role of catalyst−support interactions. For example, supramolecular coupling between cobalt phthalocyanine and oxygen-functionalized carbon nanotubes (CNTs) strengthens π-π interactions, rendering the Co center more electron-deficient and moving ΔG_{*OOH} toward the $2e^-$ ORR volcano optimum.[15] Related work shows that controlling specific oxygen functional groups at a Co-porphyrin/rGO interface pushes H_2O_2 selectivity to above 90% at the industrial-level current.[17] These findings underscore that both the electronic state of the metal center and the physicochemical properties of the substrate influence the catalytic performance.

Curvature is a significant property of layered substrates, demonstrating particularly remarkable regulation toward loaded molecular catalysts. Curved nanoscale carbons tend to induce local strain, distort the structure of loaded molecular complexes, and change the interaction between the metal center and substrate, thus modulating the catalytic performance. Previous works have linked curvature to rate enhancements and altered intermediate stabilization for macrocycle catalysts in hydrogen evolution, oxygen reduction, and CO_2 reduction.[20−22] For example, CoPc conformally bent on single-walled CNTs (high curvature) adopts distinct local geometries/electronic states relative to those of larger-diameter CNTs (lower curvature); high curvature strengthens *CO binding and enables deeper CO_2 reduction, whereas wider multiwalled CNTs favor *CO desorption.[22] Theory studies for

Received: September 9, 2025
Revised: October 17, 2025
Accepted: October 17, 2025
Published: October 22, 2025

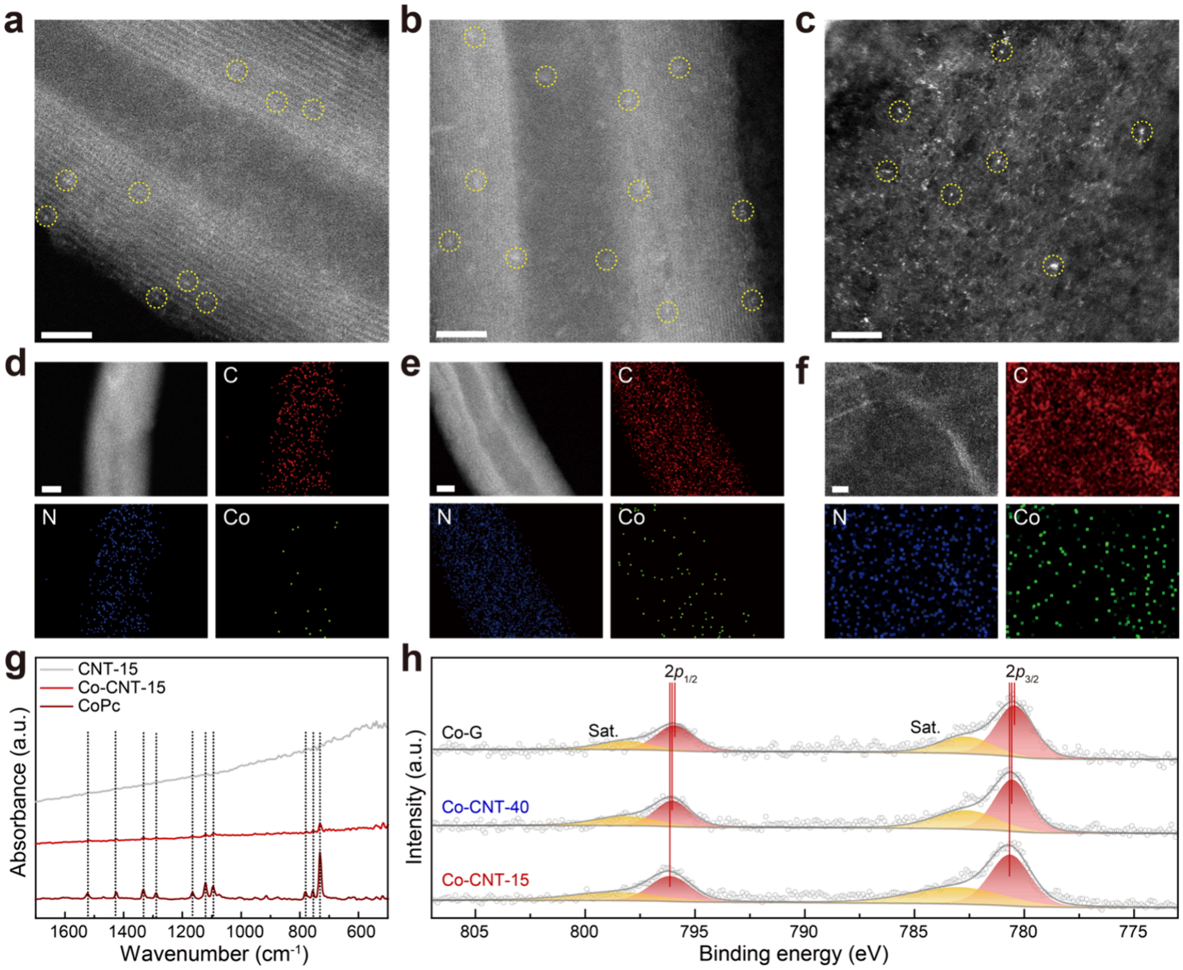

Figure 1. Characterization of the carbon material-loaded monodispersed cobalt phthalocyanine catalysts. (a−c) HAADF-STEM images of Co-CNT-15, Co-CNT-40, and Co-G, respectively. Scale bars of 2, 5, and 5 nm, respectively. (d−f) EDS mapping of Co-CNT-15, Co-CNT-40, and Co-G, respectively. Scale bars of 10, 10, and 10 nm, respectively. Co, N, and C are well distributed. (g) FTIRAS spectra of CNT-15, Co-CNT-15, and CoPc. (h) Co 2*p* XPS spectra of Co-CNT-15, Co-CNT-40, and Co-G.

Fe−N_4 sites on graphitic hosts similarly link tunable curvature to adjusted Fe−N bond lengths, *d*-band positions, and more favorable *OOH energetics, improving ORR activity over that of planar analogs.[23−25] Despite these precedents, curvature has thus far been underexploited as an independent variable for the 2e$^-$ ORR with molecular catalysts.

Herein, we decouple the influence of substrate curvature on 2e$^-$ ORR performance by anchoring monodisperse CoPc molecules on carbon supports with controlled geometries: planar graphene, 40 nm-diameter CNTs (moderate curvature), and 15 nm-diameter CNTs (high curvature). CoPc on the most curved support delivers a more than 15-fold increase in turnover frequency over the planar analog, achieving a maximum H_2O_2 productivity of 73.9 mol g_{cat}^{-1} h^{-1} above 0.6 V *versus* the reversible hydrogen electrode (*vs.* RHE) in an alkaline flow cell. To rationalize the effect of this modulation on the 2e$^-$ ORR catalytic performance, we employed theoretical calculations and *in situ* spectroscopy, revealing that the curved CoPc lowers the energy barrier of *OOH intermediate formation. For practical application, we further combined the optimal catalyst (CoPc loaded on 15 nm-diameter CNTs) with a porous solid-electrolyte (PSE) reactor to continuously yield a pure H_2O_2 solution. A 10 cm × 10 cm PSE reactor exhibited H_2O_2 selectivity >70% at a current of 10 A (with a H_2O_2 yield of ∼ 135.4 mmol h^{-1}) and was stably operated for more than 10 h. Furthermore, techno-economic analysis and life cycle assessment indicate that the cost and carbon emission of this method are competitive with those of the current technique.

For the catalyst preparation, cobalt phthalocyanine (CoPc) was immobilized by electrostatic adsorption onto carbon supports of defined curvature, i.e., planar graphene, ∼ 40 nm-diameter CNTs, and ∼ 15 nm-diameter CNTs, to yield Co-G, Co-CNT-40, and Co-CNT-15, respectively. This method is commonly used to prepare monodispersed molecular catalysts *via* *π-π* interactions.[22] Powder X-ray diffraction (XRD) revealed no reflections attributable to metallic cobalt or cobalt oxides across all of the samples, indicating the absence of crystalline Co-containing nanoparticles and supporting the molecular-level dispersion of CoPc on the hosts (Figure S1). Transmission electron microscopy (TEM) at lower magnification was used to confirm the CNT diameters (Figure S2). High-angle annular dark-field scanning transmission electron microscopy (HAADF-STEM) revealed carbon lattices without detectable Co-rich nanoparticles for Co-CNT-15, Co-CNT-40, and Co-G (Figures 1a-c). Elemental mapping by energy-dispersive X-ray spectroscopy (EDS) further confirmed the uniform and colocalized distributions of Co and N with the

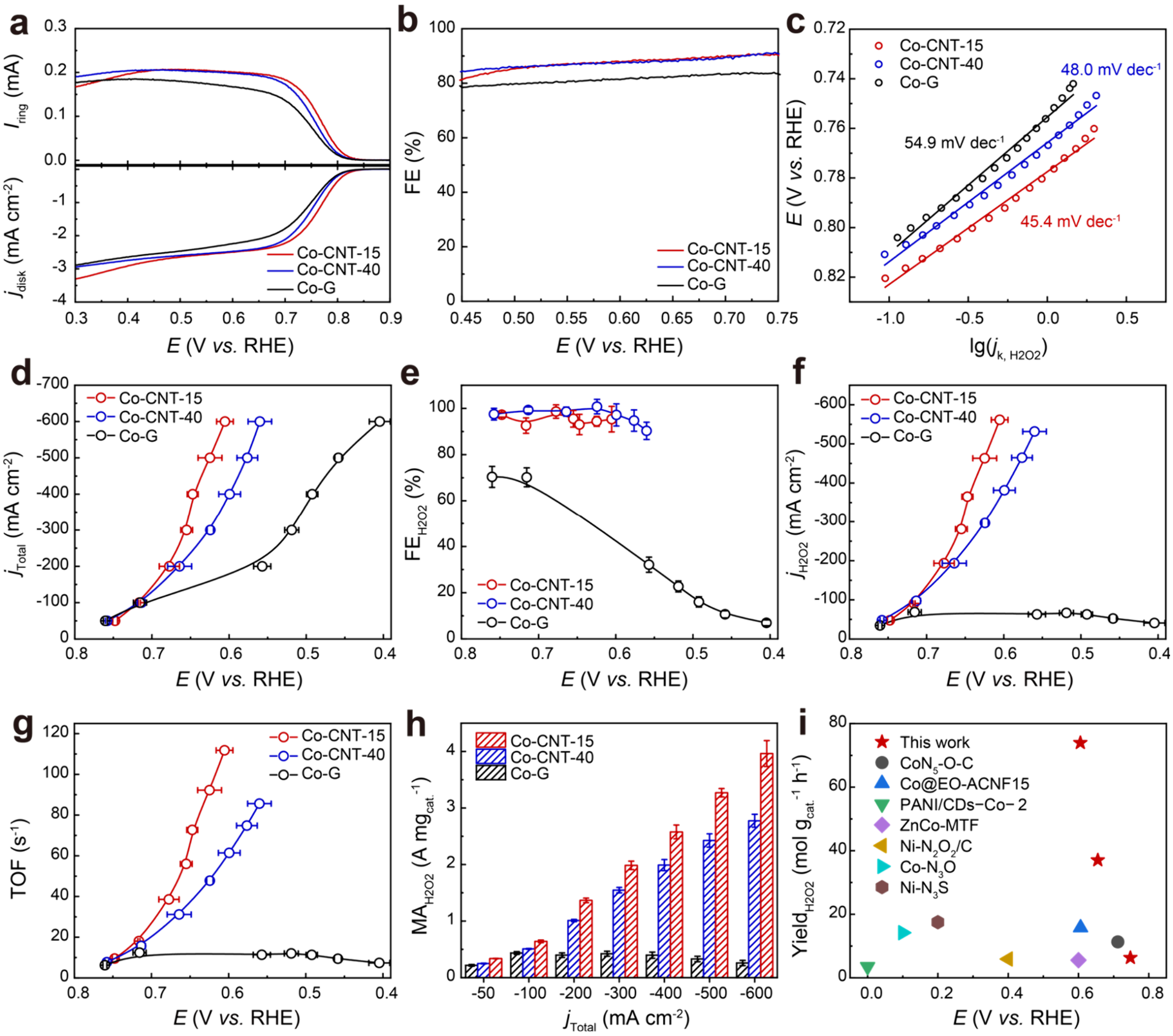

Figure 2. 2e$^-$ ORR performance evaluation of three loaded CoPc catalysts. (a) LSV curves obtained from RRDE in 0.1 M KOH. (b) Corresponding Faradaic efficiencies for H_2O_2 in RRDE. (c) Tafel analysis. (d) j_{total}-V curves in the flow cell. (e) Faradaic efficiencies for H_2O_2. (f) j_{H2O2}-V curves. (g) TOF. (h) Mass activities of Co-CNT-15, Co-CNT-40, and Co-G. Error bars represent the standard deviation of measurements based on three independent samples. (i) Comparison of H_2O_2 production performance in this work with that in previous reports.

carbon framework, which was consistent with the spatially homogeneous loading of the molecular macrocycle rather than phase-segregated domains (Figures 1d-f). Fourier-transform infrared absorption spectroscopy (FTIRAS) confirmed that the characteristic CoPc vibrational features were retained upon immobilization, whereas these bands were absent in the pristine support samples and coincided with those of the CoPc powder controls, confirming the integrity of the phthalocyanine macrocycle on both the CNT and graphene hosts (Figure 1g and Figures S3a-b). X-ray photoelectron spectroscopy (XPS) of the Co 2p region revealed progressive positive shifts in the 2$p_{3/2}$ and 2$p_{1/2}$ components from Co-G to Co-CNT-40 to Co-CNT-15 (Figure 1h and Figure S4), indicating increased electron withdrawal at the Co center and stronger metal—support coupling with increasing curvature. Collectively, these results verify monodisperse CoPc anchored on systematically curved carbons and establish curvature-dependent modulation of the Co electronic structure.

The 2e$^-$ ORR activity of CoPc on carbon substrates of differing curvatures was first assessed by a rotating ring disk electrode (RRDE) in 0.1 M KOH. The calibrated collection efficiency was 0.37 (Figure S5). Measurements of the selectivity and electron transfer number confirmed that the 2e$^-$ ORR was the dominant process on all three catalysts (Figure S6). Linear sweep voltammograms (Figure 2a) show onset potentials that shift to more positive values as the substrate curvature increases, which is consistent with a decreasing overpotential. The bare CNT-15 support displays negligible 2e$^-$ ORR activity (Figure S7), confirming that CoPc provides active sites. Co-CNT-15 and Co-CNT-40 deliver similar H_2O_2 Faradaic efficiencies (FEs) exceeding 80% across the kinetically controlled region, surpassing Co-G (Figure 2b). Tafel analysis (Figure 2c) revealed a curvature-dependent kinetic advantage. The slope decreases from Co-G to Co-CNT-40 to Co-CNT-15, with Co-CNT-15 exhibiting the lowest value (45.4 mV dec^{-1}), indicating the fastest 2e$^-$ ORR kinetics. To probe performance under practical mass-transport conditions, we conducted galvanostatic tests in a gas-diffusion flow cell (Figure 2d), which mitigates O_2 solubility and diffusion limits in aqueous media. H_2O_2 was quantified colorimetrically by $Ti(SO_4)_2$ after acidification and analyzed by ultraviolet—visible spectroscopy (UV—vis, Figures S8—S10). Co-CNT-15 and Co-CNT-40 maintain FE(H_2O_2) > 90% over a wide current range, whereas Co-G shows markedly

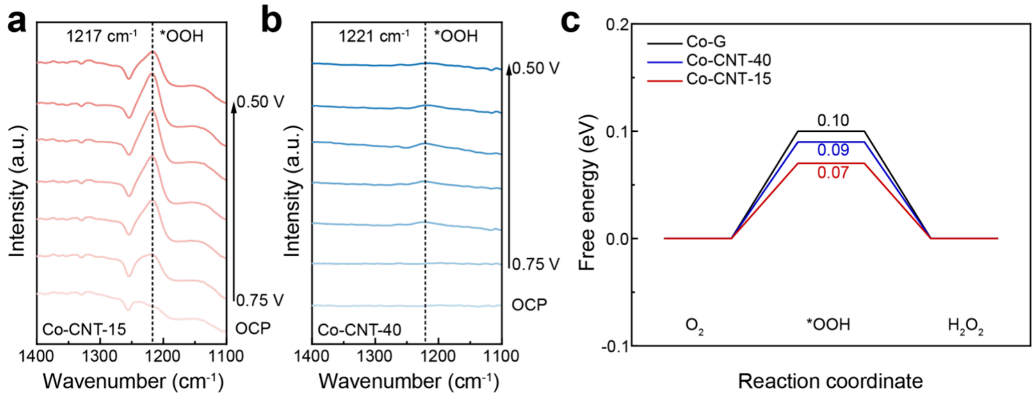

Figure 3. Mechanistic study of the substrate curve-regulated 2e$^-$ ORR process. (a and b) *In situ* ATR-SEIRAS of Co-CNT-15 and Co-CNT-40, respectively, at various potentials over the 2e$^-$ ORR. (c) Free energy diagrams of 2e$^-$ ORR coordinates over CoPc sites on substrates with different curves.

lower selectivity at higher overpotentials (Figure 2e). Consistent with the RRDE trends, Co-CNT-15 achieves higher partial current densities to H_2O_2 at lower overpotentials than Co-CNT-40 and Co-G (Figure 2f). Moreover, the 2e$^-$ ORR performance of the carbon supports in the flow cell was also investigated to exclude the influence of the substrate (Figure S11). Postoperation characterization confirmed the integrity of the catalyst. HAADF-STEM revealed no CoPc agglomeration for any sample (Figure S12), and the XPS Co 2*p* features remained unchanged after flow-cell testing (Figure S13). FTIRAS also revealed that the characteristic fingerprints of the CoPc molecule are still clearly identifiable in all three samples (Figure S14). To exclude the effects of Co mass loading, we examined the Co contents of the three catalysts *via* inductively coupled plasma-optical emission spectroscopy (ICP-OES, Table S1). Then, we normalized the 2e$^-$ ORR activity and calculated the turnover frequency (TOF) and mass activity for rigorous comparison (Figures 2g-h). The resulting metrics show that Co-CNT-15 delivers the highest intrinsic performance, with a maximum turnover frequency of 113.9 s^{-1} and a mass activity of 3.96 A mg_{cat}^{-1}, approximately 15-fold greater than that of Co-G (Figures 2g-h). Benchmarking against representative transition-metal-based 2e$^-$ ORR catalysts (Figure 2i) indicates that the performance of Co-CNT-15 compares favorably, supporting curvature modulation as an effective strategy to enhance 2e$^-$ ORR performance (Table S2).[26−31]

We then investigated how substrate curvature modulates the 2e$^-$ ORR activity. In alkaline electrolytes, the two-electron oxygen reduction reaction generally proceeds through four elementary steps (Figure S15): oxygen adsorption on the active site to form adsorbed *OO; the first proton−electron transfer from water to generate *OOH; a second proton−electron transfer to form $*H_2O_2$; and the desorption of hydrogen peroxide from the active site. The formation and stabilization of *OOH govern both the kinetics and selectivity toward the 2e$^-$ ORR in this pathway. We first used *in situ* Raman spectroscopy to track surface intermediates on Co-CNT-15 and Co-CNT-40. A potential-dependent band at ∼ 841 cm^{-1} appeared for both catalysts, which was assigned to adsorbed *OOH (Figure S16).[32] We further employed *in situ* electrochemically attenuated total reflection surface-enhanced infrared absorption spectroscopy (ATR-SEIRAS) to verify intermediate formation on all three catalysts (Figures 3b and S17). A band in the 1217−1225 cm^{-1} region, attributable to the O−O stretching mode of adsorbed *OOH, is detected for each catalyst.[33] On Co-CNT-15, this band emerges at 0.75 V *vs.* RHE, whereas on Co-CNT-40 and Co-G, it appears only at more negative potentials, which is consistent with their higher onset overpotentials. In addition, increasing the substrate curvature results in a shift of the ν(O−O) band to lower wavenumbers, which is consistent with slight O−O bond weakening and stronger adsorption of *OOH. Together with the Raman data, these results identify *OOH formation and stabilization as curvature-sensitive kinetic step. Density functional theory calculations were also conducted to rationalize these spectroscopic trends. We computed Gibbs free-energy profiles for the oxygen-to-hydrogen-peroxide sequence on cobalt phthalocyanine supported on graphitic substrates of planar, moderate, and high curvature that emulate Co-G, Co-CNT-40, and Co-CNT-15, respectively. The calculated free-energy diagrams show that a higher curvature lowers the free-energy change for *OOH formation, with the smallest barrier in the Co-CNT-15 model (Figure 3c). This result aligns with the *in situ* Raman and infrared observations. Together, spectroscopy and theory provide convergent evidence that increasing the substrate curvature strengthens *OOH stabilization and lowers its formation barrier. This curvature-induced tuning of the cobalt electronic environment accounts for the earlier onset, faster kinetics, and higher hydrogen peroxide selectivity observed on the highly curved supports.

We further assessed the long-term stability of Co-CNT-15 for the 2e$^-$ ORR at a high current density in a three-electrode flow cell reactor. We conducted the test in alkaline media with a 0.6 cm^2 gas diffusion electrode using the same method as before (Figure S18). At a current density of 200 mA cm^{-2}, the reactor operated for 154 h, maintaining over 90% of H_2O_2 FE for more than 120 h. This demonstrates the robust stability of Co-CNT-15 in a conventional flow cell. For on-site production of purified hydrogen peroxide, reactor design is as critical as catalyst design. Conventional liquid-electrolyte reactors typically require downstream desalting and purification, adding cost and complexity.[34] To directly generate a salt-free product, we adopted a porous solid-electrolyte (PSE) architecture comprising a catalyst-loaded gas-diffusion cathode for the 2e$^-$ ORR and an iridium-oxide-coated titanium mesh anode for the oxygen evolution reaction.[35] The electrodes are separated by a layered assembly of a proton-exchange membrane, a porous PSE microsphere layer, and an anion-exchange membrane. During operation, protons from the anode and HO_2^- from the

https://doi.org/10.1021/acs.nanolett.5c04538
Nano Lett. 2025, 25, 16013−16019

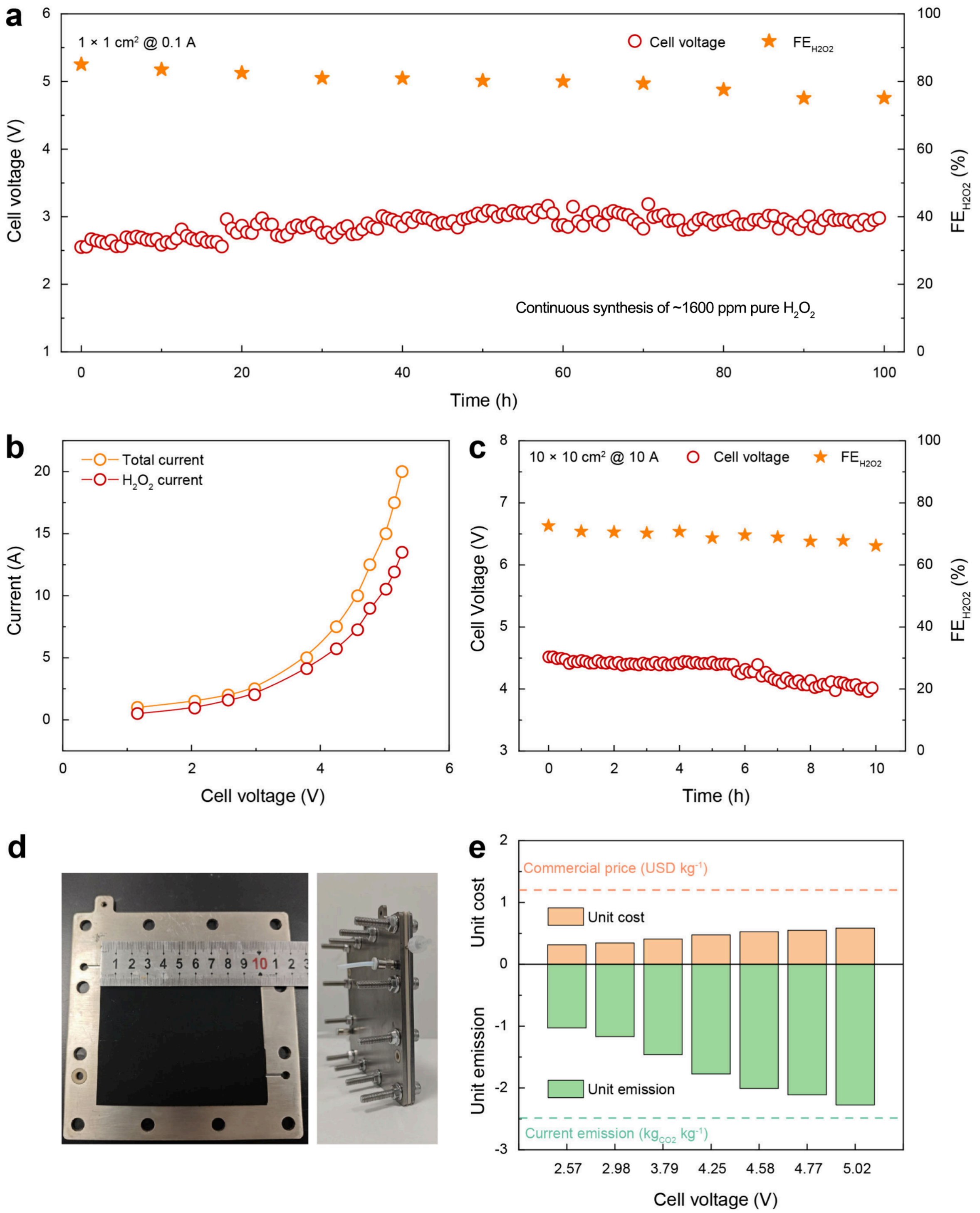

Figure 4. Pure H_2O_2 production in porous solid-electrolyte reactors using Co-CNT-15. (a) Continuous synthesis of an ∼1600 ppm pure H_2O_2 solution in a 1 cm^2 PSE reactor with a current of 0.1 A and a deionized water flow rate of 30 mL h^{-1}. (b) *j*-*V* curves. (c) Stability test at 10 A for pure H_2O_2 synthesis in a 100 cm^2 PSE reactor. (d) Digital images of the 100 cm^2 PSE reactor. (e) Techno-economic analysis and life cycle assessment of pure H_2O_2 production in a 100 cm^2 PSE reactor compared with the current commercial price and CO_2 emission.

cathode recombine in the middle layer to form H_2O_2, which is then carried away by a flow of deionized water. To evaluate the potential of Co-CNT-15 in this configuration, we assembled a 1 cm^2 PSE reactor for pure H_2O_2 production (Figure 4a and Figure S19). The device was continuously operated for 100 h, generating an ∼ 1,600 ppm of H_2O_2 solution. Notably, the cell voltage of the PSE reactor remained stable, and the H_2O_2 FE was maintained above 75%, indicating the excellent durability of this system.

Furthermore, to increase the H_2O_2 yield, we scaled up the PSE reactor with an electrode area of 10 cm × 10 cm (Figures 4b-d). As a result, a maximum H_2O_2 current of 13.5 A (∼251.8 mmol h^{-1}) was achieved (Figure 4b). Moreover, the Faradaic efficiency for H_2O_2 was maintained at over 70% after 10 h of operation at a current of 10 A (∼135.4 mmol h^{-1}, Figure 4c).

https://doi.org/10.1021/acs.nanolett.5c04538
Nano Lett. 2025, 25, 16013−16019

We further perform techno-economic analysis (TEA) and life cycle assessment (LCA) to evaluate the production cost and carbon emission of our system, respectively (Figure 4e and Notes S1 and S2). Our rough estimation yields a minimum cost of 0.31 USD $\mathrm{kg_{H2O2}}^{-1}$ and a minimum carbon emission of 1.02 $\mathrm{kg_{CO2}}$ $\mathrm{kg_{H2O2}}^{-1}$, which are competitively lower than those of the current process (~1.20 USD $\mathrm{kg_{H2O2}}^{-1}$ and 2.49 $\mathrm{kg_{CO2}}$ $\mathrm{kg_{H2O2}}^{-1}$).

In conclusion, we demonstrate that substrate-curvature modulation is an effective strategy for designing carbon-supported molecular catalysts for the 2e$^-$ ORR. Compared with its planar analog, the high-curvature catalyst Co-CNT-15 exhibited a 15-fold increase in turnover frequency and mass activity, achieving a H_2O_2 TOF of 113.9 s^{-1}. *In situ* spectroscopy and DFT calculations revealed that curvature stabilizes the *OOH intermediate, enhancing activity and selectivity. When integrated into a 10 cm × 10 cm solid-state-electrolyte reactor, the catalyst enabled pure H_2O_2 production at 135.4 mmol h^{-1} with stable operation over 10 h. Techno-economic and life-cycle analyses confirmed the competitiveness of this approach over the conventional anthraquinone process, highlighting its potential for practical application. This work underscores the critical role of support geometry in catalysis, opening new avenues for the rational design of advanced electrocatalytic systems.

■ ASSOCIATED CONTENT

Supporting Information

The Supporting Information is available free of charge at https://pubs.acs.org/doi/10.1021/acs.nanolett.5c04538.

Detailed methods (synthesis, characterization, and electrochemistry) and corresponding additional data (PDF)

■ AUTHOR INFORMATION

Corresponding Authors

Tingting Zheng − *School of Materials and Energy, University of Electronic Science and Technology of China, Chengdu 611731, P. R. China*; Email: ttzheng@uestc.edu.cn

Chuan Xia − *School of Materials and Energy, University of Electronic Science and Technology of China, Chengdu 611731, P. R. China*; orcid.org/0000-0003-4526-159X; Email: chuan.xia@uestc.edu.cn

Authors

Chunxiao Liu − *School of Materials and Energy, University of Electronic Science and Technology of China, Chengdu 611731, P. R. China*; orcid.org/0000-0002-6217-4482

Qiuxu Chen − *School of Materials and Energy, University of Electronic Science and Technology of China, Chengdu 611731, P. R. China*

Zhaoyang Chen − *School of Materials and Energy, University of Electronic Science and Technology of China, Chengdu 611731, P. R. China*; orcid.org/0000-0002-1547-698X

Jinge Wang − *School of Materials and Energy, University of Electronic Science and Technology of China, Chengdu 611731, P. R. China*

Haoyuan Wang − *School of Materials and Energy, University of Electronic Science and Technology of China, Chengdu 611731, P. R. China*; orcid.org/0009-0003-7667-8547

Laihao Luo − *School of Materials and Energy, University of Electronic Science and Technology of China, Chengdu 611731, P. R. China*; orcid.org/0009-0000-0421-088X

Xu Li − *School of Materials and Energy, University of Electronic Science and Technology of China, Chengdu 611731, P. R. China*; orcid.org/0000-0001-7577-4957

Qiu Jiang − *School of Materials and Energy, University of Electronic Science and Technology of China, Chengdu 611731, P. R. China*; orcid.org/0000-0002-2408-198X

Complete contact information is available at: https://pubs.acs.org/10.1021/acs.nanolett.5c04538

Author Contributions

C.L. and Q.C. contributed equally to this work. C.X., T.Z., and C.L. designed the study. Q.C. and H.W. synthesized the catalysts. C.L., Z.C., and L.L. conducted the material characterization and *in situ* experiments. Q.C. and J.W. evaluated the catalytic performance. Q.J. and X.L. helped analyze the data and provided suggestions. C.X., T.Z., and C.L. wrote the paper. All of the authors discussed the results and contributed to the manuscript.

Notes

The authors declare no competing financial interest.

■ ACKNOWLEDGMENTS

The authors acknowledge the National Key Research and Development Program of China (2024YFB4105700), the National Natural Science Foundation of China (52171201, 22322201, 22278067, 22308050, and 22301031), and the Natural Science Foundation of Sichuan Province (2025NSFJQ0017 and 24NSFSC6168). The authors appreciate the Analysis and Testing Center, University of Electronic Science and Technology of China, for their technical support.

■ REFERENCES

(1) Hydrogen Peroxide Market by Grade (90% H_2O_2, 35% H_2O_2, 6 to 10% H_2O_2, 3% H_2O_2), Application, End-use Industry (Pulp & Paper, Food & Beverage, Water Treatment, Textiles & Laundry, Oil & Gas, Healthcare, Electronics), & Region - Global Forecast to 2027. Markets and Markets Research Private Ltd., 2022.

(2) Campos-Martin, J. M.; Blanco-Brieva, G.; Fierro, J. L. G. Hydrogen Peroxide Synthesis: An Outlook beyond the Anthraquinone Process. *Angew. Chem., Int. Ed.* **2006**, *45* (42), 6962−6984.

(3) Ciriminna, R.; Albanese, L.; Meneguzzo, F.; Pagliaro, M. Hydrogen Peroxide: A Key Chemical for Today's Sustainable Development. *ChemSusChem* **2016**, *9* (24), 3374−3381.

(4) Yi, Y.; Wang, L.; Li, G.; Guo, H. A Review on Research Progress in the Direct Synthesis of Hydrogen Peroxide from Hydrogen and Oxygen: Noble-Metal Catalytic Method, Fuel-Cell Method and Plasma Method. *Catal. Sci. Technol.* **2016**, *6* (6), 1593−1610.

(5) Yang, S.; Verdaguer-Casadevall, A.; Arnarson, L.; Silvioli, L.; Čolić, V.; Frydendal, R.; Rossmeisl, J.; Chorkendorff, I.; Stephens, I. E. L. Toward the Decentralized Electrochemical Production of H2O2: A Focus on the Catalysis. *ACS Catal.* **2018**, *8* (5), 4064−4081.

(6) Perry, S. C.; Pangotra, D.; Vieira, L.; Csepei, L.-I.; Sieber, V.; Wang, L.; Ponce de León, C.; Walsh, F. C. Electrochemical Synthesis of Hydrogen Peroxide from Water and Oxygen. *Nat. Rev. Chem.* **2019**, *3* (7), 442−458.

(7) Wang, N.; Ma, S.; Zuo, P.; Duan, J.; Hou, B. Recent Progress of Electrochemical Production of Hydrogen Peroxide by Two-Electron Oxygen Reduction Reaction. *Adv. Sci.* **2021**, *8* (15), 2100076.

(8) Wang, Y.; Waterhouse, G. I. N.; Shang, L.; Zhang, T. Electrocatalytic Oxygen Reduction to Hydrogen Peroxide: From Homogeneous to Heterogeneous Electrocatalysis. *Adv. Energy Mater.* **2021**, *11* (15), 2003323.

(9) Deng, Z.; Choi, S. J.; Li, G.; Wang, X. Advancing H_2O_2 Electrosynthesis: Enhancing Electrochemical Systems, Unveiling Emerging Applications, and Seizing Opportunities. *Chem. Soc. Rev.* **2024**, *53*, 8137−8181.

(10) Mazzucato, M.; Facchin, A.; Parnigotto, M.; Durante, C. New and Revised Aspects of the Electrochemical Synthesis of Hydrogen Peroxide: From Model Electrocatalytic Systems to Scalable Materials. *ACS Catal.* **2024**, *14* (9), 6369−6403.

(11) Zhang, X.; Yang, X.; Su, B.; Gu, Y.; Yang, B.; Li, Z.; Zhang, Q.; Lei, L.; Dai, L.; Hou, Y. Membrane Electrode Assembly for Hydrogen Peroxide Electrosynthesis. *Nat. Rev. Clean Technol.* **2025**, *1*, 413−431.

(12) Cheng, K.; Liu, C.; Wang, Y.; Jiang, Q.; Zheng, T.; Li, X.; Xia, C. Design of Noble Metal Catalysts and Reactors for the Electrosynthesis of Hydrogen Peroxide. *Acta Phys. -Chim. Sin.* **2025**, *41*, 100112.

(13) Yu, Z.; Deng, H.; Yao, Q.; Zhao, L.; Xue, F.; He, T.; Hu, Z.; Huang, W.; Pao, C.; Yang, L.; Huang, X. Selective and Durable H_2O_2 Electrosynthesis Catalyst in Acid by Selenization Induced Straining and Phasing. *Nat. Commun.* **2024**, *15*, 9346.

(14) Liu, C.; Yu, Z. X.; She, F. X.; Chen, J. X.; Liu, F. Z.; Qu, J. T.; Cairney, J. M.; Wu, C. C.; Liu, K. L.; Yang, W. J.; Zheng, H. L.; Chen, Y.; Li, H.; Wei, L. Heterogeneous Molecular Co-N-C Catalysts for Efficient Electrochemical H_2O_2 Synthesis. *Energy Environ. Sci.* **2023**, *16* (2), 446−459.

(15) Lee, B.-H.; Shin, H.; Rasouli, A. S.; Choubisa, H.; Ou, P.; Dorakhan, R.; Grigioni, I.; Lee, G.; Shirzadi, E.; Miao, R. K.; Wicks, J.; Park, S.; Lee, H. S.; Zhang, J.; Chen, Y.; Chen, Z.; Sinton, D.; Hyeon, T.; Sung, Y.-E.; Sargent, E. H. Supramolecular Tuning of Supported Metal Phthalocyanine Catalysts for Hydrogen Peroxide Electrosynthesis. *Nat. Catal.* **2023**, *6*, 234−243.

(16) Sun, L.; Jin, X.; Su, T.; Fisher, A. C.; Wang, X. Conjugated Nickel Phthalocyanine Derivatives for Heterogeneous Electrocatalytic H_2O_2 Synthesis. *Adv. Mater.* **2024**, *36* (17), 2306336.

(17) Chen, Y.; Zhen, C.; Chen, Y.; Zhao, H.; Wang, Y.; Yue, Z.; Wang, Q.; Li, J.; Gu, M. D.; Cheng, Q.; Yang, H. Oxygen Functional Groups Regulate Cobalt-Porphyrin Molecular Electrocatalyst for Acidic H_2O_2 Electrosynthesis at Industrial-Level Current. *Angew. Chem., Int. Ed.* **2024**, *63* (34), No. e202407163.

(18) Yang, H.; Guo, N.; Xi, S.; Yin, J.; Song, T.; Xiao, Y.; Duan, L.; Zhang, C.; Wang, L. Scalable H_2O_2 Production *via* O_2 Reduction Using Immobilized Vanadyl Phthalocyanine. *Angew. Chem., Int. Ed.* **2025**, *64* (32), No. e202509079.

(19) Chen, S.; Luo, T.; Li, X.; Chen, K.; Fu, J.; Liu, K.; Cai, C.; Wang, Q.; Li, H.; Chen, Y.; Ma, C.; Zhu, L.; Lu, Y.-R.; Chan, T.-S.; Zhu, M.; Cortés, E.; Liu, M. Identification of the Highly Active Co-N_4 Coordination Motif for Selective Oxygen Reduction to Hydrogen Peroxide. *J. Am. Chem. Soc.* **2022**, *144* (32), 14505−14516.

(20) Wang, Y.; Bao, Z.; Shi, M.; Liang, Z.; Cao, R.; Zheng, H. The Role of Surface Curvature in Electrocatalysts. *Chem. - Eur. J.* **2022**, *28*, No. e202102915.

(21) She, F.; Guo, Z.; Liu, F.; Yu, Z.; Chen, J.; Fan, Y.; Lei, Y.; Chen, Y.; Li, H.; Wei, L. Curvature-Dependent Electrochemical Hydrogen Peroxide Synthesis Performance of Oxidized Carbon Nanotubes. *ACS Catal.* **2024**, *14* (14), 10928−10938.

(22) Su, J.; Musgrave, C. B.; Song, Y.; Huang, L.; Liu, Y.; Li, G.; Xin, Y.; Xiong, P.; Li, M. M.-J.; Wu, H.; Zhu, M.; Chen, H. M.; Zhang, J.; Shen, H.; Tang, B. Z.; Robert, M.; Goddard, W. A.; Ye, R. Strain Enhances the Activity of Molecular Electrocatalysts *via* Carbon Nanotube Supports. *Nat. Catal.* **2023**, *6* (9), 818−828.

(23) Li, J.; Xia, W.; Guo, Y.; Qi, R.; Xu, X.; Jiang, D.; Wang, T.; Sugahara, Y.; He, J.; Yamauchi, Y. Surface Curvature Effect on Single-Atom Sites for the Oxygen Reduction Reaction: A Model of Mesoporous MOF-Derived Carbon. *Chem. Eng. J.* **2023**, *477*, 146841.

(24) Sui, H.; Guo, Q.; Xiang, M.; Kong, X.; Zhang, J.; Ding, S.; Su, Y. Theoretical Insights of Curvature Effects of FeN_4-Doped Carbon Nanotubes on ORR Activity. *J. Phys. Chem. Lett.* **2024**, *15* (32), 8257−8264.

(25) Li, J.-K.; Zhao, H.; Zhang, Y.; Ma, J.-J.; Wang, F.-F.; Zhao, S.-N.; Li, J.; Zang, S.-Q. *In Situ* Electron Tomography Insights into the Curvature Effect of a Concave Surface on Fe Single Atoms for Durable Oxygen Reaction. *Adv. Sci.* **2025**, *12* (6), 2412387.

(26) Wang, Y.; Shi, R.; Shang, L.; Waterhouse, G. I. N.; Zhao, J.; Zhang, Q.; Gu, L.; Zhang, T. High-Efficiency Oxygen Reduction to Hydrogen Peroxide Catalyzed by Nickel Single-Atom Catalysts with Tetradentate N_2O_2 Coordination in a Three-Phase Flow Cell. *Angew. Chem., Int. Ed.* **2020**, *59* (31), 13057−13062.

(27) Zhang, W.; Choi, J. W.; Kim, S.; Le, T. T.; Nandy, S.; Hwang, C.-K.; Paek, S. Y.; Byeon, A.; Chae, K. H.; Lee, S. Y.; Kim, S. H.; Song, H.; Kim, J.; Oh, J.; Lee, J. W.; Han, S. S.; Kim, J. M. Penta Nitrogen Coordinated Cobalt Single Atom Catalysts with Oxygenated Carbon Black for Electrochemical H_2O_2 Production. *Appl. Catal. B: Environ.* **2023**, *331*, 122712.

(28) Zhou, Y.; Gu, X.; Wu, J.; Huang, H.; Shao, M.; Liu, Y.; Kang, Z. Efficient Synthesis of H_2O_2 *via* Oxygen Reduction over PANI Driven by Kinetics Regulation of Carbon Dots. *Appl. Catal. B: Environ.* **2023**, *322*, 122105.

(29) Hwang, C.-K.; Kim, S.; Yoon, K. R.; Le, T. T.; Hoang, C. V.; Choi, J. W.; Zhang, W.; Paek, S. Y.; Lee, C. H.; Lee, J. H.; Chae, K. H.; Jeong, S.; Lee, S. Y.; Ju, B.-K.; Kim, S. H.; Han, S. S.; Kim, J. M. Arc Plasma-Deposited Co Single-Atom Catalysts Supported on an Aligned Carbon Nanofiber for Hydrogen Peroxide Electrosynthesis and an Electro-Fenton Process. *Carbon Energy* **2024**, *6* (11), No. e582.

(30) Li, Z.-M.; Zhang, C.-Q.; Liu, C.; Zhang, H.-W.; Song, H.; Zhang, Z.-Q.; Wei, G.-F.; Bao, X.-J.; Yu, C.-Z.; Yuan, P. High-efficiency Electroreduction of O_2 into H_2O_2 over ZnCo Bimetallic Triazole Frameworks Promoted by Ligand Activation. *Angew. Chem., Int. Ed.* **2024**, *63* (2), No. e202314266.

(31) Liu, W.; Chen, R.; Sang, Z.; Li, Z.; Nie, J.; Yin, L.; Hou, F.; Liang, J. A Generalized Coordination Engineering Strategy for Single-Atom Catalysts toward Efficient Hydrogen Peroxide Electrosynthesis. *Adv. Mater.* **2024**, *36* (38), 2406403.

(32) Wang, Y.-H.; Le, J.-B.; Li, W.-Q.; Wei, J.; Radjenovic, P. M.; Zhang, H.; Zhou, X.-S.; Cheng, J.; Tian, Z.-Q.; Li, J.-F. *In Situ* Spectroscopic Insight into the Origin of the Enhanced Performance of Bimetallic Nanocatalysts towards the Oxygen Reduction Reaction (ORR). *Angew. Chem., Int. Ed.* **2019**, *58* (45), 16062−16066.

(33) Cao, P.; Quan, X.; Nie, X.; Zhao, K.; Liu, Y.; Chen, S.; Yu, H.; Chen, J. G. Metal Single-Site Catalyst Design for Electrocatalytic Production of Hydrogen Peroxide at Industrial-Relevant Currents. *Nat. Commun.* **2023**, *14* (1), 172.

(34) Zhang, X.; Xia, Y.; Xia, C.; Wang, H. Insights into Practical-Scale Electrochemical H_2O_2 Synthesis. *Trends Chem.* **2020**, *2* (10), 942−953.

(35) Xia, C.; Xia, Y.; Zhu, P.; Fan, L.; Wang, H. Direct Electrosynthesis of Pure Aqueous H_2O_2 Solutions up to 20% by Weight Using a Solid Electrolyte. *Science* **2019**, *366* (6462), 226−231.